

# **Stress Intensity Factors in the Third-Stage Fan Disk of the TF-30 Turbine Engine**

**R.J. SANFORD**

*Ocean Technology Division*

**and**

**J.W. DALLY**

*University of Maryland*

**May 15, 1978**



**NAVAL RESEARCH LABORATORY  
Washington, D.C.**

REPORT DOCUMENTATION PAGE		READ INSTRUCTIONS BEFORE COMPLETING FORM
1. REPORT NUMBER NRL Report 8202	2. GOVT ACCESSION NO.	3. RECIPIENT'S CATALOG NUMBER
4. TITLE (and Subtitle) STRESS INTENSITY FACTORS IN THE THIRD-STAGE FAN DISK OF THE TF-30 TURBINE ENGINE		5. TYPE OF REPORT & PERIOD COVERED Final report on one phase of a continuing NRL Problem
		6. PERFORMING ORG. REPORT NUMBER
7. AUTHOR(s) R. J. Sanford and J. W. Dally		8. CONTRACT OR GRANT NUMBER(s)
9. PERFORMING ORGANIZATION NAME AND ADDRESS Naval Research Laboratory Washington, D.C. 20375		10. PROGRAM ELEMENT, PROJECT, TASK AREA & WORK UNIT NUMBERS NRL Problem F01-29 Project A5365360-Q582
11. CONTROLLING OFFICE NAME AND ADDRESS Department of the Navy Naval Air Systems Command Washington, D.C. 20361		12. REPORT DATE May 15, 1978
		13. NUMBER OF PAGES 24
14. MONITORING AGENCY NAME & ADDRESS (if different from Controlling Office)		15. SECURITY CLASS. (of this report)  Unclassified
		15a. DECLASSIFICATION/DOWNGRADING SCHEDULE
16. DISTRIBUTION STATEMENT (of this Report)  Approved for public release; distribution unlimited		
17. DISTRIBUTION STATEMENT (of the abstract entered in Block 20, if different from Report)		
18. SUPPLEMENTARY NOTES		
19. KEY WORDS (Continue on reverse side if necessary and identify by block number) Failure analysis Photoelasticity Stress analysis Turbine engines		
20. ABSTRACT (Continue on reverse side if necessary and identify by block number) A photoelastic determination of the mixed-mode stress-intensity factors in a scale model of the third-stage fan disk of the TF-30 turbine engine has been performed. A series of 23 tests were conducted to obtain isochromatic fringe patterns at the tip of a simulated crack as it was incrementally extended through the lug along the observed failure path. The isochromatic fringe patterns were analyzed by employing a newly developed method which permits determination of both opening and shearing mode stress-intensity factors $K_I$ and $K_{II}$ in the presence of far-field stresses $\sigma_{ox}$ . Although		

(Continued)

DD FORM 1473  
1 JAN 73EDITION OF 1 NOV 65 IS OBSOLETE  
S/N 0102-LF-014-6601

## 20. ABSTRACT (Continued)

both  $K_I$  and  $K_{II}$  varied as the crack extended from its initiation point to its turning point, the effective stress intensity factor  $K_{eff}$ , equal to the square root of the sum of the squares of  $K_I$  and  $K_{II}$ , remained essentially constant over most of the length of the fracture path. After the crack turns, the propagation is predominantly mode I and the value of  $K_{eff}$  increases dramatically with increasing crack length.

## CONTENTS

INTRODUCTION .....	1
EXPERIMENTAL PROCEDURE .....	3
METHODS OF ANALYSIS .....	4
Classical Approach .....	5
Selected-Line Approach .....	7
Least-Squares Approach .....	8
VERIFICATION OF METHODS .....	10
ANALYSIS OF DATA .....	10
SCALING FROM MODEL TO PROTOTYPE .....	13
ERROR ESTIMATE .....	15
REFERENCES .....	17
APPENDIX A — Program MXDMD4 .....	18
APPENDIX B — Program MXDMD5 .....	20

## STRESS INTENSITY FACTORS IN THE THIRD-STAGE FAN DISK OF THE TURBINE ENGINE

### INTRODUCTION

Several failures of the TF-30 turbojet engine used in the F-14 aircraft have been attributed to the initiation and growth of fatigue cracks in the third-stage fan disk at the dovetail region shown in Fig. 1. It is generally believed that these cracks are associated with an intermittent high-frequency engine resonance and/or load fluctuations due to engine power or speed changes. Since the operational static load is already high, only moderate fluctuations are required for crack initiation followed by fatigue growth. In either case, a reduction in the static stress level extends fatigue life. To this end, an experimental stress analysis of the dovetail was performed by Parks and Sanford<sup>(1)</sup> using two-dimensional photoelastic models. The photoelastic analysis showed a stress concentration factor of 5.2 in the disk fillet. The high concentration of tensile stress in the fillet plus the fretting action at the edge of the bearing surface are the two primary factors affecting crack initiation.

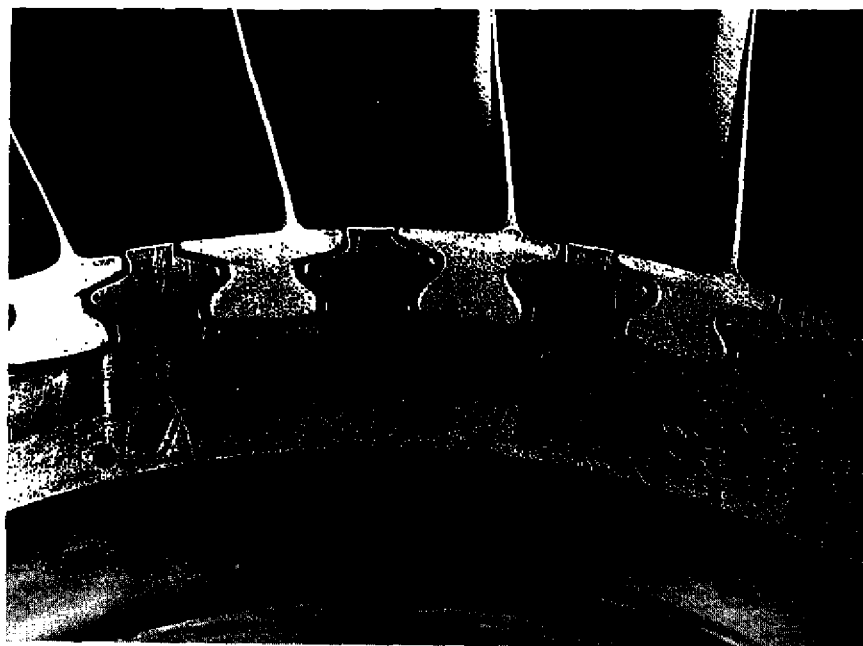


Fig. 1 — TF-30 third-stage blade/disk  
dovetail region

Fatigue cracking occurs in a reproducible manner in numerous lugs on each disk. A typical disk removed from service was carefully examined at NRL, and cracks were observed in 15 of the 36 lugs. In each instance, the crack initiates at or near the junction of the fillet and bearing area of the disk lugs as illustrated in Fig. 2. After initiation, the crack extends upward across the lug until it approaches the upper fillet, where a compressive stress field exists. At this point the crack turns through an angle of 45 degrees and propagates across the upper region of the lug as shown in Fig. 3.

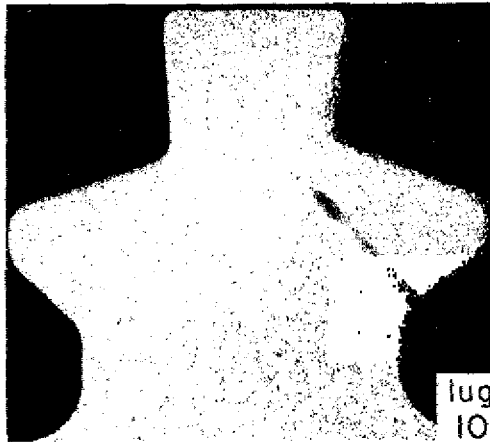


Fig. 2 — Typical fatigue crack in a disk removed from service



Fig. 3 — Final phase of crack extension after the crack turns

This report provides a fracture analysis of a crack as it extends from the initiation point into the lug. Of particular interest is the stress-intensity factor or the strain energy release rate at the crack tip as the crack propagates into the complex stress field associated with the dovetail region. Knowing the stress intensity factor along the path of the crack will enable a prediction to be made of the propagation life of the fatigue crack from the Paris<sup>(2)</sup> cyclic-growth relationship

$$da/dN = C \Delta K^n, \quad (1)$$

where  $da/dN$  is the incremental crack extension per cycle,  $\Delta K$  is the range in stress intensity factor, and  $n$  and  $C$  are material constants.

To determine the stress intensity factor, two-dimensional photoelastic models 3.409 times the size of the dovetail region of the disk were used. Artificial cracks were introduced in the models by sawing. The cracks were extended incrementally along the known fracture path, and isochromatic fringe patterns were recorded for each crack length.

The isochromatic patterns in the neighborhood of the crack tip indicated that the stress field was of the mixed-mode type and that a far-field stress  $\sigma_{ox}$  parallel to the crack was of significant magnitude. As a method of determining the opening stress intensity factor  $K_I$  and the shearing-mode stress intensity factor  $K_{II}$  from isochromatic fringe loops under these conditions was not available, it was necessary to develop a data-analysis procedure. This was accomplished by using a modified near-field solution for the central crack problem to obtain a non-

linear equation relating  $K_I$ ,  $K_{II}$ , and  $\sigma_{ox}$  to the fringe order  $N$  and the fringe position  $(r, \theta)$  relative to the crack tip. Solution of this nonlinear equation and the extraction of  $K_I$ ,  $K_{II}$ , and  $\sigma_{ox}$  was obtained using the Newton-Raphson iterative method combined with a least-squares method to minimize error due to inaccuracies in measuring fringe parameters. The results obtained for  $K_I$  and  $K_{II}$  were accurate to 10 to 15 percent based on individual determinations and to about 5 to 7 percent based on mean-value estimates when several determinations were made.

Results from the model analysis for  $K_I$  and  $K_{II}$  were scaled to the prototype based on a centrifugal load of 24,900 lb (111 kN) applied to the prototype. An effective stress intensity factor  $K_{eff}$ , related to  $K_I$  and  $K_{II}$ , was determined as a function of crack length.

## EXPERIMENTAL PROCEDURE

The experimental approach was similar to the approach used by Parks and Sanford<sup>(1)</sup> in their photoelastic stress analysis. A complete description of the model geometry, the loading fixture, and model manufacturing methods is contained in Ref. 1. The models used in this study were made from the same templates as employed by Parks and Sanford and had in-plane dimensions 3.409 times the prototype dimensions.

The models were fabricated from Homalite 100\* sheets 0.255 in. (6.48 mm) thick. A crack was simulated in the model by using a fine-pitched jewelers saw 0.018 in. (0.5 mm) thick with 40 teeth per inch. The crack tip was sharpened with a swiss jewelers file\*\* with a radius of about 0.008 in. (0.2 mm).

The model was loaded in a sodium diffused-light polariscope, and isochromatic fringe patterns were photographically recorded. The crack was extended incrementally by sawing and filing; then the loading and photographing sequence was repeated. A total of 23 combinations of load and crack length were photographed.

Typical isochromatic fringe patterns obtained for three lengths of cracks are illustrated in Fig. 4. An enlargement of the fringe loops at the crack tip is presented in Fig. 5. Inspection of



Fig. 4 — Typical isochromatic fringes for crack extension in the disk dovetail

\*G & L Industries, Wilmington, Delaware.

\*\*Grobet Vallorbe No. 6 jewelers file.

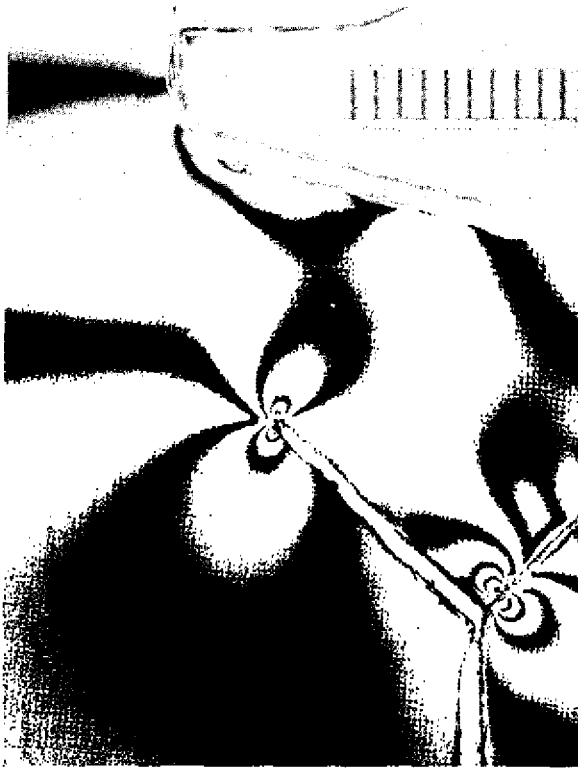


Fig. 5 — Enlargement showing details of the fringe loops at the crack tip

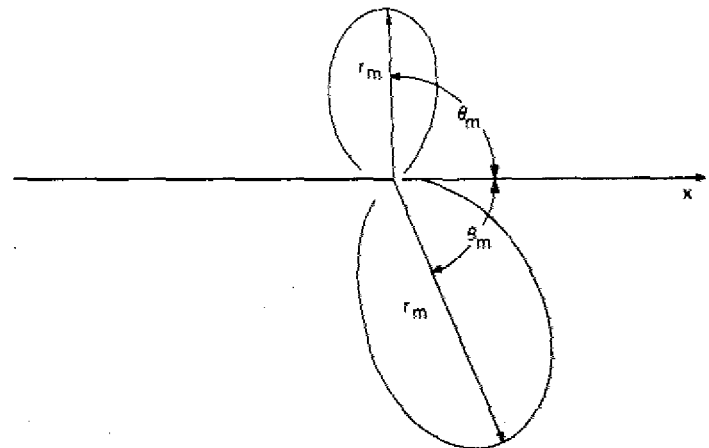


Fig. 6 — Characteristic shape of upper and lower loops

these fringe patterns shows that the loop tilt angle  $\theta_m$  (defined in Fig. 6) and the maximum radius  $r_m$  associated with the fringe loops above and below the crack line are not the same. Thus the cracks are propagating in a mixed-mode field with both  $K_I$  and  $K_{II}$  affecting fatigue crack extension.

#### METHODS OF ANALYSIS

A method to determine mixed-mode stress intensity factors from isochromatic fringe loops has previously been developed by Smith and Smith<sup>(3)</sup>. Their method, which neglects the



nonsingular far-field stress  $\sigma_{ox}$ , can be applied only when the axes of the upper and lower fringe loops lie along a common line. Examination of Fig. 5 indicates that this condition is not satisfied for the problem being considered here. For this reason it was necessary to extend the method of analysis to include the  $\sigma_{ox}$  term.

For a crack subjected to both tensile and shearing loads the stress field in the neighborhood of the crack tip can be approximated<sup>(4)</sup> as

$$\begin{aligned}\sigma_x &= \frac{1}{\sqrt{2\pi r}} \left[ K_I \cos \frac{\theta}{2} \left( 1 - \sin \frac{\theta}{2} \sin \frac{3\theta}{2} \right) - K_{II} \sin \frac{\theta}{2} \left( 2 + \cos \frac{\theta}{2} \cos \frac{3\theta}{2} \right) \right] - \sigma_{ox}, \\ \sigma_y &= \frac{1}{\sqrt{2\pi r}} \left[ K_I \cos \frac{\theta}{2} \left( 1 + \sin \frac{\theta}{2} \sin \frac{3\theta}{2} \right) + K_{II} \sin \frac{\theta}{2} \cos \frac{\theta}{2} \cos \frac{3\theta}{2} \right], \\ \tau_{xy} &= \frac{1}{\sqrt{2\pi r}} \left[ K_I \sin \frac{\theta}{2} \cos \frac{\theta}{2} \cos \frac{3\theta}{2} + K_{II} \cos \frac{\theta}{2} \left( 1 - \sin \frac{\theta}{2} \sin \frac{3\theta}{2} \right) \right],\end{aligned}\quad (2)$$

where the coordinates are measured from the crack tip.

The maximum in-plane shear stress  $\tau_m$  is related to the Cartesian components of stress by

$$(2\tau_m)^2 = (\sigma_y - \sigma_x)^2 + (2\tau_{xy})^2. \quad (3)$$

The stress-optic law in photoelasticity which relates the fringe order  $N$  to the maximum in-plane shear stress is

$$2\tau_m = Nf_\sigma/h, \quad (4)$$

where  $f_\sigma$  is the material fringe value and  $h$  is the model thickness.

Substituting Eqs. (2) and (4) into (3) gives

$$\begin{aligned}(Nf_\sigma/h)^2 &= \frac{1}{2\pi r} [(K_I \sin \theta + K_{II} \cos \theta)^2 + (K_{II} \sin \theta)^2] \\ &\quad + \frac{2\sigma_{ox}}{\sqrt{2\pi r}} \sin \frac{\theta}{2} [K_I \sin \theta (1 + 2 \cos \theta) \\ &\quad + K_{II} (1 + 2 \cos^2 \theta + \cos \theta)] + \sigma_{ox}^2.\end{aligned}\quad (5)$$

The size and shape of the isochromatic fringe loops are related to  $K_I$ ,  $K_{II}$ , and  $\sigma_{ox}$  through Eq. (5). It is possible to use this relation in two ways — first, to assume that  $K_I$ ,  $K_{II}$ , and  $\sigma_{ox}$  are known and to use Eq. (5) to determine the geometry of fringe loops of a given order or, second, to assume the geometry of the fringe loop is known and to use Eq. (5) to determine  $K_I$ ,  $K_{II}$ , and  $\sigma_{ox}$ .

Thus Eq. (5) forms the basis of all of the methods used to determine  $K_I$ ,  $K_{II}$ , and  $\sigma_{ox}$  from isochromatic fringe patterns. In this analysis three approaches were followed in developing solutions. In each approach the set of equations to be solved was nonlinear in the unknowns  $K_I$ ,  $K_{II}$ , and  $\sigma_{ox}$ . These equations were solved using the Newton-Raphson method as applied to systems of equations<sup>(5)</sup>. Each of the approaches will be described.

### Classical Approach

In the first determination of  $K_I$  and  $\sigma_{ox}$  from symmetrical fringe loops, performed by Irwin<sup>(6)</sup>, it was noted that, for closed fringe loops near the crack tip, a point exists where

$$\frac{\partial \tau_m}{\partial \theta} = 0. \quad (6)$$

This point was assigned coordinates  $(r_m, \theta_m)$ . This relation gave Irwin a second equation to use with a simplified form of Eq. (5) ( $K_{II}$  terms eliminated) and enabled him to solve for  $K_I$  and  $\sigma_{ox}$  in terms of the fringe order  $N$  and the position parameters  $r_m$  and  $\theta_m$ .

This approach can also be used in the mixed-mode mode analysis by using information from two loops in the near-field of the crack. Differentiating Eq. (5) with respect to  $\theta$ , setting  $\theta = \theta_m$  and  $r = r_m$ , and using Eq. (6) gives

$$\begin{aligned} f(K_I, K_{II}, \sigma_{ox}) &= \frac{1}{2\pi r_m} (K_I^2 \sin 2\theta_m + 4K_I K_{II} \cos 2\theta_m - 3K_{II}^2 \sin 2\theta_m) \\ &\quad + \frac{2\sigma_{ox}}{\sqrt{2\pi r_m}} \left\{ \sin \frac{\theta_m}{2} [K_I(\cos \theta_m + 2\cos 2\theta_m) - K_{II}(2\sin 2\theta_m + \sin \theta)] \right\} \\ &\quad + \frac{1}{2} \cos \frac{\theta_m}{2} \left\{ [K_I(\sin \theta_m + \sin 2\theta_m) + K_{II}(2 + \cos 2\theta_m + \cos \theta_m)] \right\} \\ &= 0, \end{aligned} \quad (7)$$

where the coordinates  $r_m$  and  $\theta_m$  define the point on any fringe loop which is farthest removed from the crack tip, as illustrated in Fig. 6. Rewriting Eq. (5) in a form suitable for use with the Newton-Raphson method gives

$$\begin{aligned} g(K_I, K_{II}, \sigma_{ox}) &= \frac{1}{2\pi r_m} [(K_I \sin \theta_m + K_{II} \cos \theta_m)^2 + (K_{II} \sin \theta_m)^2] \\ &\quad + \frac{2\sigma_{ox}}{\sqrt{2\pi r_m}} \sin \frac{\theta_m}{2} [K_I \sin \theta_m (1 + 2\cos \theta_m) \\ &\quad + K_{II}(1 + 2\cos^2 \theta_m + \cos \theta_m)] + \sigma_{ox}^2 - (N_m f_\sigma/h)^2 = 0, \end{aligned} \quad (8)$$

where  $N_m$  is the fringe order corresponding to the point  $(r_m, \theta_m)$ .

When the classical approach is used, the stress intensity factors  $K_I$  and  $K_{II}$  and the remote stress  $\sigma_{ox}$  are determined from isochromatic data taken from two points — one on each of two fringes. In concept any two loops can be used; however, in practice more accurate results are obtained if one fringe is taken from the set of loops above the crack line and the other fringe is taken from the set of loops below the crack line.

Substituting the radii  $r_m$  and the angles  $\theta_m$  from these two loops into Eq. (7) gives two independent relations in terms of the parameters of interest. The third equation is obtained by using Eq. (8) with data from either the upper or the lower loop. The three equations obtained in this manner are of the form

$$\begin{aligned} f_u(K_I, K_{II}, \sigma_{ox}) &= 0, \\ f_l(K_I, K_{II}, \sigma_{ox}) &= 0, \\ g_u(K_I, K_{II}, \sigma_{ox}) &= 0, \end{aligned} \quad (9)$$

where the subscripts  $u$  and  $l$  refer to upper and lower loops respectively.

Although Eqs. (9) can be solved in closed form, the algebra becomes quite involved, and a simpler approach using a numerical procedure based on the Newton-Raphson method was employed. To describe the Newton-Raphson method, consider an arbitrary function  $h_k$  of the form

$$h_k(K_I, K_{II}, \sigma_{ox}) = 0, \quad (10)$$

where  $k = 1, 2$ , and  $3$ . If initial estimates are made for  $K_I$ ,  $K_{II}$ , and  $\sigma_{ox}$  and substituted into Eq. (10), the equality is not satisfied, since the estimates are in error. To correct the estimates, a series of iterative equations based on a Taylor series expansion of  $h_k$  are written as

$$(h_k)_{i+1} = (h_k)_i + \left[ \frac{\partial h_k}{\partial K_I} \right]_i \Delta K_I + \left[ \frac{\partial h_k}{\partial K_{II}} \right]_i \Delta K_{II} + \left[ \frac{\partial h_k}{\partial \sigma_{ox}} \right]_i \Delta \sigma_{ox}, \quad (11)$$

where the subscript  $i$  refers to the  $i$ th iteration step.  $\Delta K_I$ ,  $\Delta K_{II}$ , and  $\Delta \sigma_{ox}$  are corrections to the previous estimates. The corrections are determined so that  $(h_k)_{i+1} = 0$ , and thus Eq. (11) gives

$$\left[ \frac{\partial h_k}{\partial K_I} \right]_i \Delta K_I + \left[ \frac{\partial h_k}{\partial K_{II}} \right]_i \Delta K_{II} + \left[ \frac{\partial h_k}{\partial \sigma_{ox}} \right]_i \Delta \sigma_{ox} = -(h_k)_i. \quad (12)$$

Applying Eqs. (12) to Eqs. (9) and solving for the correction terms  $\Delta K_I$ ,  $\Delta K_{II}$ , and  $\Delta \sigma_{ox}$  yields, in matrix notation,

$$\begin{bmatrix} \Delta K_I \\ \Delta K_{II} \\ \Delta \sigma_{ox} \end{bmatrix} = - \begin{bmatrix} \frac{\partial f_u}{\partial K_I} & \frac{\partial f_u}{\partial K_{II}} & \frac{\partial f_u}{\partial \sigma_{ox}} \\ \frac{\partial f_l}{\partial K_I} & \frac{\partial f_l}{\partial K_{II}} & \frac{\partial f_l}{\partial \sigma_{ox}} \\ \frac{\partial g_u}{\partial K_I} & \frac{\partial g_u}{\partial K_{II}} & \frac{\partial g_u}{\partial \sigma_{ox}} \end{bmatrix}^{-1} \begin{bmatrix} f_u \\ f_l \\ g_u \end{bmatrix}_i. \quad (13)$$

The corrected values of  $K_I$ ,  $K_{II}$ , and  $\sigma_{ox}$  are given by

$$\begin{aligned} (K_I)_{i+1} &= (K_I)_i + \Delta K_I, \\ (K_{II})_{i+1} &= (K_{II})_i + \Delta K_{II}, \\ (\sigma_{ox})_{i+1} &= (\sigma_{ox})_i + \Delta \sigma_{ox}. \end{aligned} \quad (14)$$

The convergence of this method is rapid, and usually four or five iterations are sufficient for obtaining precise estimates of  $K_I$ ,  $K_{II}$ , and  $\sigma_{ox}$ . A computer program written in BASIC, with a file name MXDMD4, was prepared to compute  $K_I$ ,  $K_{II}$ , and  $\sigma_{ox}$  according to Eqs. (13) and (14). This program is listed in Appendix A.

#### Selected-Line Approach

It is possible to simplify Eq. (5) by considering only the isochromatic data along the line defined by  $\theta = \pi$ . Then Eq. (5) reduces to

$$(Nf_{\sigma}/h)^2 = \frac{4 K_{II}^2}{2\pi r} + \frac{4 K_{II} \sigma_{ox}}{\sqrt{2\pi r}} + \sigma_{ox}^2, \quad (15)$$

which is independent of  $K_I$ . Equation (15) can be written as

$$Nf_{\sigma}/h = \pm \left[ \frac{2 K_{II}}{\sqrt{2\pi r}} + \sigma_{ox} \right]. \quad (16)$$

The negative sign is selected, because  $K_{II} < 0$  for isochromatic intercepts with the  $\theta = \pi$  line.\* Consider two isochromatics  $N_1 > N_2$ , which intercept the  $\theta = \pi$  line at positions  $r_1$  and  $r_2$  as shown in Fig. 7 and select the minus-sign solution in Eq. (16). Then

$$\sigma_{ox} = -\frac{N_1 f_\sigma}{h} - \frac{2 K_{II}}{\sqrt{2\pi r_1}} \quad (17a)$$

and

$$\sigma_{ox} = -\frac{N_2 f_\sigma}{h} - \frac{2 K_{II}}{\sqrt{2\pi r_2}}. \quad (17b)$$

Subtracting Eq. (17b) from Eq. (17a) to eliminate  $\sigma_{ox}$  gives

$$K_{II} = \frac{f_\sigma}{h} \frac{\sqrt{\pi}}{2} \frac{\sqrt{r_1 r_2}}{\sqrt{r_1} - \sqrt{r_2}} (N_1 - N_2), \quad (18)$$

which is negative, since  $N_1 > N_2$  and  $r_2 > r_1$ . Finally  $\sigma_{ox}$  is obtained from Eq. (18) and Eq. (17a) as

$$\sigma_{ox} = -\frac{N_1 f_\sigma}{h} - \frac{2 K_{II}}{\sqrt{2\pi r_1}}. \quad (19)$$

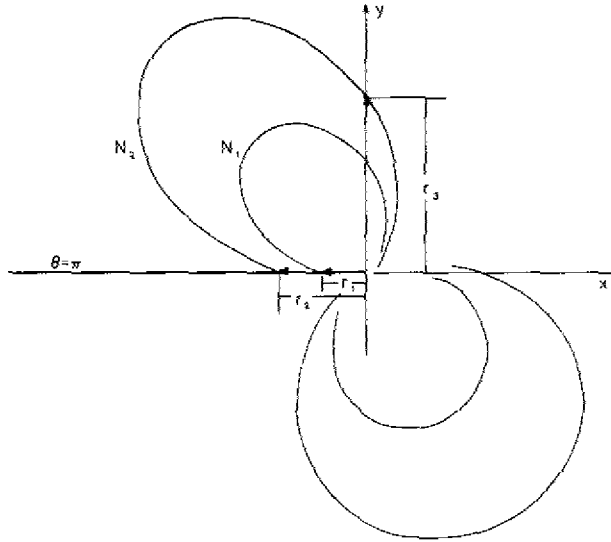


Fig. 7 — Isochromatic fringe orders  $N_1$  and  $N_2$  intersecting the line  $\theta = \pi$  (upper crack edge)

To determine  $K_I$ , reevaluate Eq. (5) with  $\theta = \pi/2$  and obtain

$$(N f_\sigma / h)^2 = \frac{1}{2\pi r} (K_I^2 + K_{II}^2) + \frac{\sigma_{ox}}{\sqrt{\pi r}} (K_I + K_{II}) + \sigma_{ox}^2. \quad (20)$$

Equation (20) is quadratic in terms of  $K_I$ ; thus

$$K_I = \frac{-b + \sqrt{b^2 - 4ac}}{2a}, \quad (21)$$

\*A similar development can be made when  $K_{II} > 0$ , except that the isochromatics intersect the lower edge of the crack at  $\theta = -\pi$ .

where

$$\begin{aligned} a &= 1/2\pi r_3, \\ b &= \sigma_{ox}/\sqrt{\pi r_3}, \\ c &= (K_I^2/2\pi r_3) + (K_{II} \sigma_{ox}/\sqrt{\pi r_3}) + \sigma_{ox}^2 - (N_3 f_\sigma/h)^2. \end{aligned} \quad (22)$$

Note that  $N_3$  and  $r_3$  are defined in Fig. 7. The plus sign is selected in front of the radical in Eq. (21), since  $K_I > 0$ .

### Least-Squares Approach

The least-squares approach fits Eq. (5) to the data at a number of arbitrary points over the fringe field in the neighborhood of the crack tip using the unknowns  $K_I$ ,  $K_{II}$ , and  $\sigma_{ox}$  as the fitting parameters. The fitting process is similar to that used in the classical approach in that the Newton-Raphson method is employed; however the least-squares approach uses data from  $k$  arbitrary points, where  $k > 3$ .

Applying the iteration scheme suggested in Eq. (12) to  $k$  equations of the form given in Eq. (8) results in an overdetermined set of linear equations in terms of the unknowns  $\Delta K_I$ ,  $\Delta K_{II}$ , and  $\Delta \sigma_{ox}$  of the form

$$\begin{bmatrix} g_1 \\ g_2 \\ \vdots \\ g_k \end{bmatrix} = - \begin{bmatrix} \frac{\partial g_1}{\partial K_I} & \frac{\partial g_1}{\partial K_{II}} & \frac{\partial g_1}{\partial \sigma_{ox}} \\ \frac{\partial g_2}{\partial K_I} & \frac{\partial g_2}{\partial K_{II}} & \frac{\partial g_2}{\partial \sigma_{ox}} \\ \vdots & \vdots & \vdots \\ \frac{\partial g_k}{\partial K_I} & \frac{\partial g_k}{\partial K_{II}} & \frac{\partial g_k}{\partial \sigma_{ox}} \end{bmatrix} \begin{bmatrix} \Delta K_I \\ \Delta K_{II} \\ \Delta \sigma_{ox} \end{bmatrix}. \quad (23)$$

For brevity rewrite the matrices in Eq. (23) as

$$[g] = [a] [\Delta K]. \quad (24)$$

It can be shown that  $[\Delta K]$  in Eq. (24) can be determined in the least-squares sense by multiplying both sides from the left by  $[a]^T$ , where  $[a]^T$  is the transpose of  $[a]$ :

$$[a]^T [g] = [a]^T [a] [\Delta K] \quad (25)$$

or

$$[d] = [c] [\Delta K], \quad (26)$$

where

$$[d] = [a]^T [g]$$

and

$$[c] = [a]^T [a].$$

Finally,

$$[\Delta K] = [c]^{-1} [d], \quad (27)$$

where  $[c]^{-1}$  is the inverse of  $[c]$ .

The solution of Eq. (27) gives  $\Delta K_I$ ,  $\Delta K_{II}$ , and  $\Delta \sigma_{ox}$ , which are used to correct initial estimates of  $K_I$ ,  $K_{II}$ , and  $\sigma_{ox}$  to obtain a better fit of the function  $g$  to the  $k$  data points. By use of the matrix operations available in BASIC, a computer program with a file name MXDMD5 was written to determine  $K_I$ ,  $K_{II}$ , and  $\sigma_{ox}$  using data from ten points over the fringe field. This program is listed in Appendix B.

### VERIFICATION OF METHODS

All three methods were verified and were found to give accurate results (to  $\pm 0.1$  percent), providing exact input data were used. The data required for verification were generated by substituting selected values of  $K_I$ ,  $K_{II}$ , and  $\sigma_{ox}$  into Eq. (5). The resulting expression was then used to determine the fringe order  $N$  at specified  $(r, \theta)$  pairs.

Analysis with real data is less accurate, because experimental errors will occur in determining the  $r$  and  $\theta$  associated with the location of a point on an isochromatic fringe. Errors in  $\theta$  of  $\pm 2$  degrees and in  $r$  of  $\pm 0.005$  in. (0.13 mm) should be expected. The errors are primarily due to difficulties in locating the crack tip at the end of the saw cut.

The classical approach is perhaps the most error prone of the three methods, since  $\theta_m$  must be determined for both the upper and lower loops. Considering the difficulty in locating the crack tip and in locating the point corresponding to  $r_m$  on both isochromatic fringe loops, errors in  $\theta_m$  of  $\pm 5$  degrees may be anticipated. An example was run with computer program MXDMD4 such that  $\theta_m$  on the upper loop was increased by 5 degrees and  $\theta_m$  on the lower loop was decreased by 5 degrees. The error in the predictions of  $K_I$ ,  $K_{II}$ , and  $\sigma_{ox}$  was 13.9, 15.6, and 38 percent respectively.

The selected-line, classical, and least-squares methods were compared by using the analytically generated point plot of the fringe pattern shown in Fig. 8. Measurements of  $r$ ,  $\theta$ , and  $N$  were taken from this point plot using the same techniques which are used with actual photoelastic fringe patterns. The data with typical measurement errors were processed, and the results of the error analysis are shown in Table 1. These results indicate that the least-squares method with the program MXDMD5 provided the most accurate estimates of  $K_I$  and  $K_{II}$ .

### ANALYSIS OF DATA

Negatives of the fringe patterns were projected in a photographic enlarger onto the data sheet shown in Fig. 9. The projected size of the image was approximately 10 times the actual model size. Five data points associated with each fringe loop were marked on the data sheet. These data points were usually at the extremity of a fringe loop, where changes in  $r$  with  $\theta$  are small and measurement error is minimized. The scale distance (5 mm) from the negative was marked on the data sheet.

Measurements were made with proportional dividers to determine the radius associated with each data point. Values of angle  $\theta$ , radius  $r$ , and fringe order  $N$  associated with ten to 40 data points were made from each negative of the isochromatic pattern.

These data were used as input for the MXDMD-5 program to determine  $K_I$ ,  $K_{II}$ , and  $\sigma_{ox}$ . Ten data points were used for each determination, five from an upper loop and five from a lower loop. When more than ten data points were available, different combinations of data sets were employed and several estimates of  $K_I$ ,  $K_{II}$ , and  $\sigma_{ox}$  were made. In these instances, averages of the individual determinations were taken. The mean values of  $K_I$ ,  $K_{II}$ , and  $\sigma_{ox}$  are presented in Table 2.

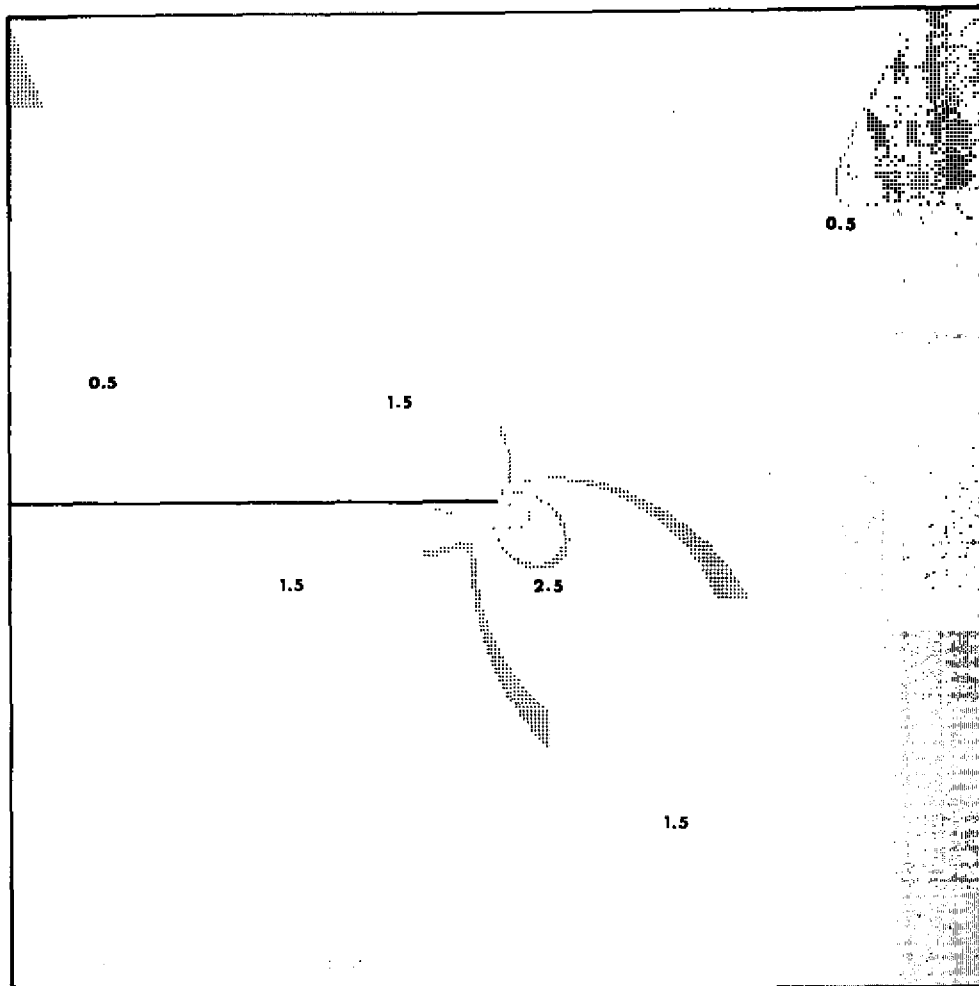
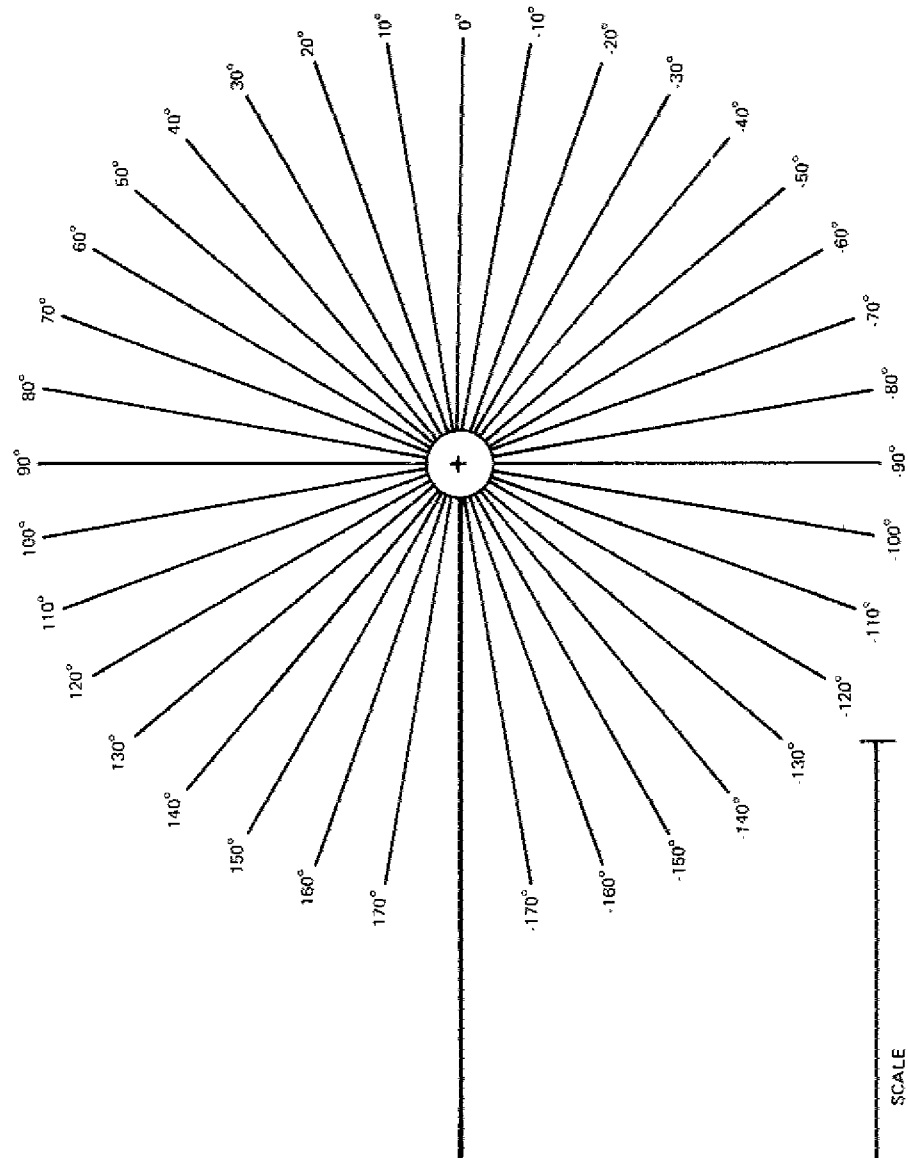


Fig. 8 — Point plot of a mixed-mode isochromatic pattern influenced by a far-field stress  
 $\sigma_{ox} K_I = 319 \text{ psi } \sqrt{\text{in.}}, K_{II} = -293 \text{ psi } \sqrt{\text{in.}}, \sigma_{ox} = 355 \text{ psi}$

Table 1 — Comparison of the three Methods  
 on the Basis of Typical Measurement Errors

	True Value	Least-Squares Method		Selected-Line Method		Classical Method	
		Predicted Value	Error (%)	Predicted value	Error (%)	Predicted Value	Error (%)
$K_I \text{ (psi}\sqrt{\text{in.)}}$	318.974	317.5	0.5	304.8	4.5	298.4	6.4
$K_{II} \text{ (psi}\sqrt{\text{in.)}}$	-293.184	-297.1	1.3	-308.2	5.1	-308.0	5.1
$\sigma_{ox} \text{ (psi)}$	354.865	345.3	2.7	380.7	7.2	357.9	0.8

FIELD	pos.in.
f <sub>σ</sub>	in.



CRACK LENGTH RECORD

Fig. 9 -- Data sheet used to record the coordinates  $(r, \theta)$  for a large number of points in a fringe field



Table 2 — Summary of Results for  $K_I$ ,  $K_{II}$ , and  $\sigma_{ox}$  for the Photoelastic Model

Record No.	Number of Readings	P Load (lb)	Crack Length (in.)	$K_I$ (psi√in.)	$K_{II}$ (psi√in.)	$\sigma_{ox}$ (psi)
Before Crack Turns						
D-2-6 & 7	1	800	0.096	573	-569	2482
D-2-8 & 9	1	1000	0.096	693	-706	2974
D-1-3	1	200	0.122	439	-216	327
D-1-4	1	200	0.185	475	-159	238
D-1-5 & 6	5	200	0.241	348	-219	377
D-1-7 & 8	6	200	0.357	318	-285	357
D-1-9 & 10	7	200	0.466	512	-203	298
D-1-11 & 12	7	200	0.622	539	-281	318
D-1-13 & 14	5	200	0.710	549	-221	134
D-1-15 & 16	3	200	0.843	392	-334	152
D-1-17 & 18	5	200	0.955	351	-444	213
After Crack Turns						
D-1-19 & 20	1	200	0.100	793	-365	370
D-1-21 & 22	3	150	0.190	782	-184	431
D-1-23 & 24	1	200	0.190	1038	-198	533
D-1-25 & 26	2	100	0.296	815	-86	131
D-1-27 & 28	1	100	0.296	786	-163	154
D-1-29 & 30	1	100	0.410	1044	244	326
D-1-31 & 32	1	100	0.518	1196	347	519

### SCALING FROM MODEL TO PROTOTYPE

Conversion of the results from the photoelastic model of the turbine disk to results which correspond to the actual prototype requires the use of a scaling relationship. The scaling equation for  $K_I$  or  $K_{II}$  is

$$(K_{I,II})_p = \sqrt{\lambda_1} \lambda_2 \lambda_3 (K_{I,II})_m, \quad (28)$$

where the subscripts  $p$  and  $m$  refer to the prototype and model respectively. The terms  $\lambda_1$ ,  $\lambda_2$ , and  $\lambda_3$  in Eq. (28) are scaling factors defined as follows:

$$\lambda_1 = \text{the in-plane scaling factor} = w_m/w_p = 3.409, \quad (29)$$

where  $w_m$  is the center-to-center dimension between two adjacent blades on the model and is 3.808 in. (96.7 mm) and  $w_p$  is the corresponding dimension on the prototype and is 1.117 in. (28.38 mm);

$$\lambda_2 = \text{the thickness scaling factor} = h_m/h_p = 0.111, \quad (30)$$

where  $h_p$  is the length of the dovetail slot and is 2.30 in. (58.34 mm) and  $h_m$  is the model thickness and is 0.255 in. (6.48 mm); and

$$\lambda_3 = \text{the load scaling factor} = P_p/P_m = 124.5, \quad (31)$$

where  $P_p = 24,900$  lb (111 kN) and  $P_m = 200$  lb (890 N).

The scaling equation for the length  $a$  of the crack is

$$a_p = a_m / \lambda_1. \quad (32)$$

These scaling relations assume that the crack in the prototype propagates in a two-dimensional manner (as through-thickness cracks with a straight front). Inspection of the fracture surface of the lugs which have been pulled from the disk, as shown in Fig. 10, indicate that the cracks propagate with three-dimensional characteristics. The cracks initiate at a point and do not extend along the entire thickness of the disk. Instead the crack front exhibits significant curvature. Because of these differences in the crack shape between the model and the prototype, the results presented here should be considered as a first approximation. More exact predictions would require three-dimensional photoelastic studies to more adequately model the crack shape.



Fig. 10 — Typical fracture surface showing the three-dimensional characteristics of a fatigue crack

Numerical values of  $K_I$  and  $K_{II}$  related to a load on the prototype of  $P_p = 24,900$  lb (111 kN) are given in Table 3 as a function of crack length  $a_p$ . Inspection of Table 3 shows that both  $K_I$  and  $K_{II}$  vary between narrow limits as the crack grows from 0 to 0.280 in. (7.1 mm) deep. To assess the influence of the combined effect of  $K_I$  and  $K_{II}$ , it is appropriate to consider the total strain energy release rate  $G$ , which is given by

$$G = G_I + G_{II}, \quad (33)$$

where, for plane strain,

$$G_I = \frac{1 - \nu^2}{E} K_I^2 \quad (34a)$$

and

$$G_{II} = \frac{1 - \nu^2}{E} K_{II}^2, \quad (34b)$$

in which  $E$  is the modulus of elasticity and  $\nu$  is Poisson's ratio.

Substituting Eqs. (34) into Eq. (33) gives

$$G = \frac{1 - \nu^2}{E} K_{eff}^2, \quad (35)$$

Table 3 — Stress Intensity Factors  $K_I$  and  $K_{II}$   
in the Third-Stage Fan-Blade/Disk  $P_p = 24,900$  lb  
Centrifugal Load

$K_I$ (ksi $\sqrt{\text{in.}}$ )	$K_{II}$ (ksi $\sqrt{\text{in.}}$ )	a (in.)	$K_{eff}$ (ksiin.)
Before Crack Turns			
3.65	-3.63	0.28	5.15
3.54	-3.60	0.028	5.05
11.20	-5.51	0.035	12.48
12.12	-4.06	0.054	12.78
8.88	-5.59	0.071	10.49
8.11	-7.27	0.105	10.89
13.06	-5.18	0.137	14.05
13.75	-7.17	0.182	15.51
14.01	-5.64	0.208	15.10
10.00	-8.52	0.247	13.14
8.96	-11.33	0.280	14.44
After Crack Turns			
20.23	-9.31	.029	22.27
26.60	-6.26	.056	27.33
41.59	-4.39	.087	41.82
40.11	-8.31	.087	40.96
53.28	12.45	.120	54.71
61.03	17.70	.151	63.54

where

$$K_{eff} = \sqrt{K_I^2 + K_{II}^2} \quad (36)$$

The effective stress intensity factor  $K_{eff}$ , which governs the rate of crack propagation  $da/dN$  according to Eq. (1), increases from zero to a value of about 14 ksi $\sqrt{\text{in.}}$  as the crack extends to a depth of about 0.100 in., as shown in Fig. 11. Continued crack extension from 0.100 to 0.280 in. occurs at nearly constant  $K_{eff}$ .

After extending a distance of 0.280 in., the crack approaches the compressive stress field near the upper fillet of the lug. The value of  $K_I$  decreases and  $|K_{II}|$  increases until the crack turns through an angle of about 45 degrees. After turning,  $K_I$  becomes dominant and  $K_{eff}$  increases markedly with further crack extension. It is believed that the rate of crack propagation will increase rapidly after the crack turns.

## ERROR ESTIMATE

In most of the cases examined here, several fringe loops were available for analysis and 30 or 40 data points could be obtained from regions on the fringe loops where  $r$  was not changing rapidly with respect to  $\theta$ . In these instances, the data could be grouped into different sets of ten data points, and multiple determinations of the  $K$  field could be made. An example of the scatter in the determination of  $K_I$ ,  $K_{II}$ , and  $\sigma_{ox}$  is shown in Table 4 for a typical set of data.

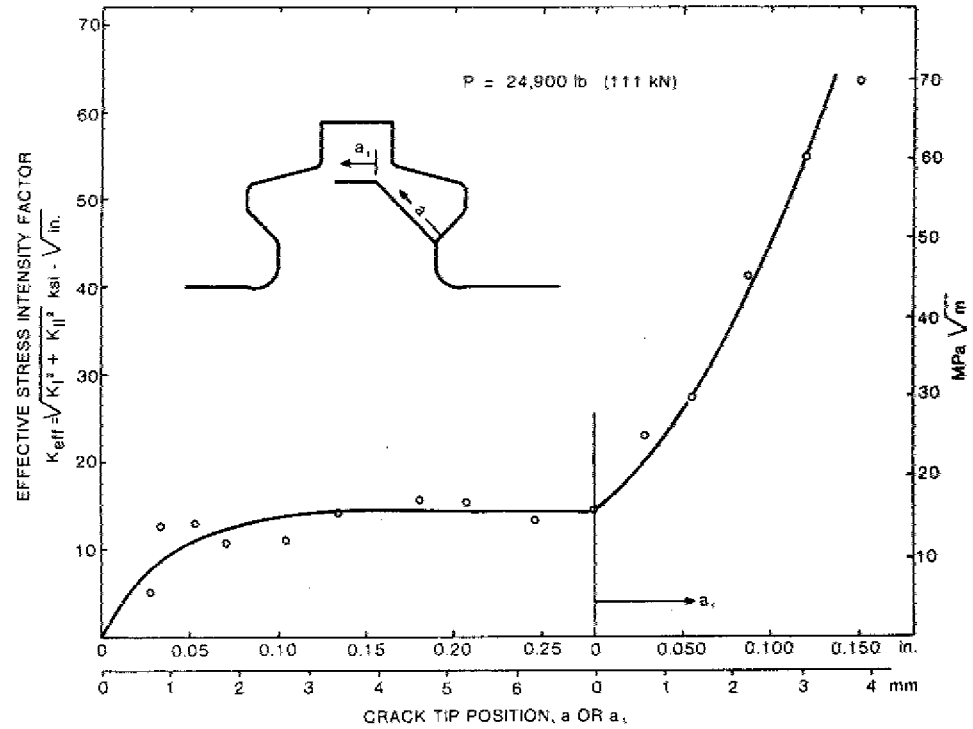


Fig. 11 — Effective stress intensity factor  $K_{eff}$  as a function of crack length  $a$ .

Table 4 — Values of  $K_I$ ,  $K_{II}$ , and  $\sigma_{ox}$  Determined with Seven Sets of Ten Data Points

	$K_I$	$K_{II}$	$\sigma_{ox}$
Seven	525.7	-203.8	296.2
sets	456.6	-257.6	321.0
of	547.4	-207.5	227.7
data	516.9	-194.8	314.2
points	444.4	-193.2	369.3
	509.7	-195.2	300.1
	583.9	-170.0	260.6
$\bar{x}$	512.1	-203.1	298.4
$S_x$	48.8	26.8	45.1
$S_x/\bar{x}$	0.095	0.132	0.151
$S_{\bar{x}}$	18.4	10.1	17.0
$S_{\bar{x}}/\bar{x}$	0.036	0.050	0.057

The mean value  $\bar{x}$ , standard deviation  $S_x$ , and coefficient of variation  $S_x/\bar{x}$  were determined and are also listed in Table 4. These statistical parameters indicate that errors in individual determinations of  $K_I$  of about  $\pm 10$  percent and in  $K_{II}$  of about  $\pm 13$  percent can be expected about 68 percent of the time. If the error is due to random causes, then the averaging process improves the accuracy. The standard deviation of the mean  $S_{\bar{x}}$  is

$$S_{\bar{x}} = S_x/\sqrt{n},$$

where  $n$  is the number of measurements.

The values of  $S_{\bar{x}}$  and  $S_x/\bar{x}$  listed in Table 4 illustrate the improvement in predictions based on mean values. In this case, errors of  $\pm 3.6$ ,  $\pm 5.0$ , and  $\pm 5.7$  percent in  $K_{I\bar{x}}$ ,  $K_{II\bar{x}}$ , and  $\sigma_{ox}$  can be anticipated 68 percent of the time. Higher errors would be anticipated 32 percent of the time.

#### REFERENCES

1. V.J. Parks and R.J. Sanford, "Experimental Stress Analysis of the TF-30 Turbine Engine Third-Stage Fan-Blade/Disk Dovetail Region," NRL Report 8149, Aug. 1977.
2. P. Paris and F. Erdogan, "A Critical Analysis of Crack Propagation Laws," ASME Trans. D **85**, 528-534 (1963).
3. D.G. Smith and C.W. Smith, "Photoelastic Determination of Mixed Mode Stress Intensity Factors", Engrg. Fract. Mech. **4** (No. 2), 357-366 (1972).
4. P.C. Paris and G.C. Sih, "Stress Analysis of Cracks," ASTM STP No. 381, pp. 30-81, 1965.
5. L.G. Kelley, *Handbook of Numerical Methods and Applications*, Addison Wesley, Reading, Mass., 1967, p. 99.
6. G.R. Irwin, discussion of the paper by A.A. Wells and D. Post, "Dynamic Stress Distribution Surrounding a Running Crack — A Photoelastic Analysis," Proc. SESA **16** (No. 1), 69-93 (1958), discussion on pp. 93-96.

Appendix A  
PROGRAM MXDMD4

```

00001 REM A PROGRAM EMPLOYING THE CLASSICAL METHOD OF ANALYSIS
00002 REM FOR DETERMINING K1,K2 AND SIGMA SUB 0X
00003 REM THE NUMERICAL ANALYSIS IS BASED ON THE NEWTON RAPHSON METHOD.
00004 REM
00009 REM CAUTION THETA FOR LOWER LOOP IS NEGATIVE.
00010 PRINT "INPUT THETA,RADIUS AND FRINGE ORDER FROM UPPER LOOP";
00015 INPUT T1,R1,N1
00020 PRINT "INPUT THETA,RADIUS AND FRINGE ORDER FROM LOWER LOOP";
00025 INPUT T2,R2,N2
00030 PRINT "INPUT MATERIAL FRINGE VALUE AND MODEL THICKNESS";
00035 INPUT P,H
00040 PRINT "INPUT INITIAL ESTIMATE OF K1";
00045 INPUT K1
00050 K2=0
00055 K3=0
00060 PRINT"NUMBER OF ITERATIONS M IS";
00065 INPUT M
00070 REM COMPUTE TRIG FUNCTIONS
00075 T1=3.14159*T1/180
00080 T2=3.14159*T2/180
00085 S0=SQRT(2*3.14159*R1)
00090 S1 =SIN(T1)
00095 S2=COS(T1)
00100 S3=SIN(T1/2)
00105 S4=COS(T1/2)
00110 S5=SQRT(2*3.14159*R2)
00115 S6=SIN(T2)
00120 S7=COS(T2)
00125 S8=SIN(T2/2)
00130 S9=COS(T2/2)
00135 REM COMPUTE COEFFICIENTS OF TAYLOR'S SERIES.
00140 A1=S1**2/S0**2
00145 A2=4*S1*S2/S0**2
00150 A3=(4*S2**2+S1**2)/S0**2
00155 A4=2*S3*S1*(1+2*S2)/S0
00160 A5=2*S3*(1+2*S2**2+S2)/S0
00165 AR=(N1*P/H)**2
00170 B1=S6**2/S5**2
00175 B2=4*S6*S7/S5**2
00180 B3=(4*S7**2+S6**2)/S5**2
00185 B4=2*S8*S6*(1+2*S7)/S5
00190 B5=2*S8*(1+2*S7**2+S7)/S5
00195 BR=(N2*P/H)**2
00200 C1=2*S1*S2/S0**2
00205 C2=4*(S2**2-S1**2)/S0**2
00210 C3=-6*S1*S2/S0**2
00215 C4=(2/S0)*(S3*(S2+2*S2**2-2*S1**2)+(.5*S4)*(S1+2*S1*S2))
00220 C5=(2/S0)*(-S3*(4*S1*S2+S1)+(.5*S4)*(2+S2**2-S1**2+S2))
00225 D1=2*S6*S7/S5**2

```

NRL REPORT 8202

```

00230 D2=4*(S7**2-S6**2)/S5**2
00235 D3=-6*S6*S7/S5**2
00240 D4=(2/S5)*(S8*(S7+2*S7**2-2*S6**2)+(5*S9)*(S6+2*S6*S7))
00245 D5=(2/S5)*(-S8*(4*S6*S7+S6)+(5*S9)*(2+S7**2-S6**2+S7))
00250 PRINT
00255 PRINT " K SUB 1    K SUB 2    SIGMA SUB 0X"
00260 PRINT K1,K2,K3
00265 DIM F(3),U(3,3),V(3,3),Y(3,3),X(3)
00270 REM BEGIN ITERATIVE SOLUTION
00275 FOR L=1 TO M
00280 F(1)=A1*K1**2+A2*K1*K2+A3*K2**2+A4*K1*K3+A5*K2*K3+K3**2-A8
00285 F(2)=B1*K1**2+B2*K1*K2+B3*K2**2+B4*K1*K3+B5*K2*K3+K3**2-B8
00290 F(3)=D1*K1**2+D2*K1*K2+D3*K2**2+D4*K1*K3+D5*K2*K3
00295 U(1,1)=2*A1*K1+A2*K2+A4*K3
00300 U(1,2)=A2*K1+2*A3*K2+A5*K3
00305 U(1,3)=A4*K1+A5*K2+2*K3
00310 U(2,1)=2*B1*K1+B2*K2+B4*K3
00315 U(2,2)=B2*K1+2*B3*K2+B5*K3
00320 U(2,3)=B4*K1+B5*K2+2*K3
00325 U(3,1)=2*D1*K1+D2*K2+D4*K3
00330 U(3,2)=D2*K1+2*D3*K2+D5*K3
00335 U(3,3)=D4*K1+D5*K2
00340 MAT V=INV(U)
00345 MAT Y=V*F
00350 MAT X=(-1)*Y
00355 K1=K1+X(1)
00360 K2=K2+X(2)
00365 K3=K3+X(3)
00370 PRINT K1,K2,K3
00375 NEXT L
00380 END

```

Appendix B  
PROGRAM MXDMD5

```

00001 REM A PROGRAM WHICH USES THE LEAST SQUARES METHOD TOGETHER WITH THE
00002 REM NEWTON RAPHSON METHOD TO DETERMINE K1,K2 AND SIGMA SUB OX
00003 REM FROM AN OVER DETERMINED SYSTEM OF EQUATIONS.
00004 REM THE PROGRAM IS WRITTEN TO ACCEPT 10 DATA POINTS.
00005 REM
00010 PRINT "INPUT INITIAL ESTIMATE OF K1"
00015 INPUT K1
00020 K2=0
00025 K3=0
00030 PRINT "INPUT DATA FOR THETA (T), RADIUS (R) AND FRINGE ORDER (N)"
00035 FOR J=1 TO 10
00040 INPUT T(J),R(J),N(J)
00045 T(J)=3.14159*T(J)/180
00050 NEXT J
00055 PRINT "MATERIAL FRINGE VALUE AND MODEL THICKNESS":
00060 INPUT P,H4
00065 REM CONVERT UNKNOWNNS TO NORMALIZED FORM.
00070 K1=K1*H4/P
00085 PRINT "SPECIFY NUMBER OF ITERATIONS":
00090 INPUT Q
00095 DIM G(10),A(10,3),K(3,10),C(3,3),D(3),U(3,3),V(3,3),X(3)
00100 PRINT " K SUB 1   K SUB 2   SIGMA SUB OX"
00105 FOR I=1 TO 10
00110 S0(I)=2*3.14159*R(I)
00115 S1(I)=SIN(T(I))
00120 S2(I)=COS(T(I))
00125 S3(I)=SIN(T(I)/2)
00130 S4(I)=COS(T(I)/2)
00135 A1(I)=(S1(I))**2/S0(I)
00140 A2(I)=4*S1(I)*S2(I)/S0(I)
00145 A3(I)=(4*(S2(I))**2+(S1(I))**2)/S0(I)
00150 A4(I)=2*S3(I)*S1(I)*(1+2*S2(I))/SQRT(S0(I))
00155 A5(I)=2*S3(I)*(1+2*(S2(I))**2+S2(I))/SQRT(S0(I))
00160 A6(I)=(N(I))**2
00165 NEXT I
00170 REM BEGIN ITERATIVE SOLUTION.
00175 FOR L=1 TO Q
00180 E1=0
00185 FOR I=1 TO 10
00190 E(I)=A5(I)*K2*K3+K3**2-A6(I)
00195 G(I)=A1(I)*K1**2+A2(I)*K1*K2+A3(I)*K2**2+A4(I)*K1*K3+E(I)
00200 A(I,1)=2*A1(I)*K1+A2(I)*K2+A4(I)*K3
00205 A(I,2)=A2(I)*K1+2*A3(I)*K2+A5(I)*K3
00210 A(I,3)=A4(I)*K1+A5(I)*K2+2*K3
00215 E1=E1+G(I)**2
00220 NEXT I
00225 MAT K=TRN(A)
00230 MAT C=K*A
00235 MAT D=K*G

```



NRL REPORT 8202

```
00240 MAT U=INV (C)
00245 MAT V=(-1)*U
00250 MAT X=V*D
00255 K1=K1+X(1)
00260 K2=K2+X(2)
00265 K3=K3+X(3)
00270 PRINT K1*P/H4;K2*P/H4;K3*P/H4
00275 NEXT L
00280 PRINT "RELATIVE ERROR"
00285 PRINT E1
00290 END
```